Catalysis Communications 177 (2023) 106656

Contents lists available at ScienceDirect

Catalysis Communications

journal homepage: www.elsevier.com/locate/catcom

Bi-based halide perovskites: Stability and opportunities in the photocatalytic approach for hydrogen evolution

Magdalena Miodyńska [a,*], Tomasz Klimczuk [b], Wojciech Lisowski [c], Adriana Zaleska-Medynska [a,*]

[a] Department of Environmental Technology, Faculty of Chemistry, University of Gdansk, 80-308 Gdansk, Poland
[b] Faculty of Applied Physics and Mathematics and Advanced Materials Center, Gdansk University of Technology, 80-233 Gdansk, Poland
[c] Institute of Physical Chemistry, Polish Academy of Science, 01-224 Warsaw, Poland

ARTICLE INFO

Keywords:
Photocatalysis
Bi-based perovskite
Lead-free perovskite
Halide perovskite
Hydrogen evolution

ABSTRACT

In this study, we successfully prepared Bi-based single perovskites of the $A_3Bi_2I_9$ type (A = Cs, Rb, MA, FA), and, for the first time, attempted to experimentally obtain double perovskites $Cs_2B'BiI_6$ type (B′ = Ag, Au, In, Cu). Despite the premises available in theoretical studies, our research has proven the impossibility of the existence of double perovskites of this type. Nevertheless, both types of obtained materials were subjected to detailed analysis of their physicochemical features and photocatalytic abilities in the hydrogen evolution reaction. This study proved the stability of the $Cs_3Bi_2I_9$ in HI electrolyte compared to the methanolic solution, with this phenomenon resulting in almost 36 times higher photoactivity.

1. Introduction

Heterogeneous photocatalysis is a reaction that has potential applications in reducing atmospheric CO_2 emissions, water and air treatment, and producing hydrogen gas, which is a clean energy source alternative to fossil fuels [1,2]. The key to realizing these benefits is to determine and optimize the parameters for photocatalytic performance to increase the efficiency of the reaction, especially in the field of visible light, which constitutes the majority of the spectrum of widely available cheap solar irradiation [1–3]. One of the most important factors that scientists worldwide are working on is the type of photocatalyst used during the reaction [1,2]. To date, the most well-known and widely used photocatalyst, along with a number of structural and surface modifications, is TiO_2; however, its wide bandgap (~3.2 eV [1,4]) and conduction band potential significantly limit its effective application in photocatalytic reactions aimed at generating hydrogen [3–5]. Nevertheless, TiO_2 has been applied in the photoreaction of H_2 evolution following the hydrolysis of ammonia borane [6], glycerol or methanol photoreforming [7,8], or by using typical sacrificial agents such as lactic acid [9], sulfide/sulfite electrolyte [10,11], triethanolamine [11,12], and formic acid [13].

However, the potential of a group of halide perovskite semiconductors for photoinduced hydrogen evolution has recently been explored because of their strong light absorption coefficient and fast charge mobility. In addition, their iodo-derivatives have the appropriate potential of the conduction band for reduction process with the release of gaseous hydrogen [14,15]. Most are narrow-band semiconductors; thus, it is possible to excite them in the presence of low-energy visible irradiation [15]. Moreover, the best-known in this group are perovskites containing lead in their structure, which strongly increases the toxicity of the whole compound and thus significantly limits their use in photocatalytic processes [16]. Therefore, because the Bi trivalent isoelectronic ions and divalent Pb ions have a similar valence shell with a $6s^2$ electron pair and exhibit similar ionic radii, Bi-based halide perovskites seem to be excellent substitutes for lead-derived perovskites, as much more stable and eco-friendly analogs [14,16,17]. The greatest limitation for the use of halide perovskites in photocatalytic reactions is their lack of resistance to contact with aqueous electrolytes [18]. Ignoring that fact, some studies have been conducted on the application of perovskites in aqueous reactions of hydrogen photogeneration [19]: $DMASnI_3$ (DMA: dimethylammonium cation), a perovskite stable in water, was tested in pure water as the electrolyte [20]; composite g-C_3N_4 with a $CsPbI_3$ structure was photoapplied in aqueous TEOA electrolyte [21]; $CsPbBr_3$ stabilized by doping with Zn^{2+} cations was tested in aqueous sulfide/sulfite solution [22], and $CsPbBr_3$ stabilized by encapsulation with polyaniline was also tested in water media [23].

* Corresponding authors.
E-mail addresses: magdalena.miodynska@ug.edu.pl (M. Miodyńska), adriana.zaleska-medynska@ug.edu.pl (A. Zaleska-Medynska).

https://doi.org/10.1016/j.catcom.2023.106656
Received 2 March 2023; Accepted 27 March 2023
Available online 29 March 2023

Nevertheless, milestones in the application of halide perovskites in photocatalytic reactions include the use of an appropriate halide acid (HBr, HI, HCl, or a mixture) as an electrolyte to generate hydrogen in the presence of halide perovskites [15]. This finding allowed for the effective use of such photocatalysts and the termination of their decomposition in contact with water [15]. To date, a number of halide perovskites (including $MAPbBr_{3-x}I_x$ [24], $MAPbI_3$ [25,26], $TiO_2/MAPbI_3$ composite [27], $MAPbI_3/MoS_2$ composite [28], black phosphorus/$MAPbI_3$ composite [29], $MAPbI_3$/CoP composite [30], Ni_3C decorated $MAPbI_3$ [31], $TiO_2/MAPbI_3$ composite [32], Ti_3C_2 MXene/$MAPbI_3$ composite [33], $Mo_2C/MAPbI_3$ composite [34], MoC/$MAPbI_3$ composite [35], $MA_3Bi_2I_9$ [36], $Cs_3Bi_{2x}Sb_{2-2x}I_9$ [37], $Cs_3Bi_2I_9$ [38], $Cs_2AgBiBr_6$ [39], NiCoP/$Cs_2AgBiBr_6$ composite [40], DMA_3BiI_6 [41] and $Cs_2AgBiBr_6$/rGO composite [42]) have been used in reactions with halogen acids. Most of them belong to Pb-based single perovskites, and not many other variants have been developed, for example, bi-analogs. Our motivation to obtain novel Pb-free, Bi-based double perovskites was based on theoretical studies that proved the possibility of the existence of such structures [43–47].

According to our previous work [48] and based on knowledge about the highest conduction band potential (CB) for iodide analogs over the same group of perovskites [49], here, we devised the synthesis of single Bi-based iodo-perovskites with different A cations ($A_3Bi_2I_9$ where A indicates Cs, Rb, methylammonium (MA), and formamidinium (FA) cation) and determined their photocatalytic properties in the hydrogen evolution reaction. Furthermore, for the first time, the photoactivity to hydrogen evolution was examined for Rb_3Bi_2I9 and $FA_3Bi_2I_9$. For the most active sample ($Cs_3Bi_2I_9$), we introduced additional cations during the synthesis procedure to form a double perovskite structure. Thus, for the first time, an attempt to obtain double $Cs_2B'BiI_6$ type perovskites (where B′ means Ag, Au, In, or Cu) was made, and their photocatalytic ability in the hydrogen evolution reaction was studied. Furthermore, all the obtained photocatalysts were comprehensively characterized in terms of morphological, structural, and surface properties, combined with their photoactivity. In addition, the mechanism of the photocatalytic reaction in two different electrolytes (aqueous 10% MeOH and HI/H_3PO_2) was thoroughly investigated. The increased activity of halide perovskites in the HI electrolyte was directly related to the stability of these compounds in this environment.

2. Experimental

2.1. Materials and instruments

For the preparation of single and double perovskites, chalcogenide salts as precursors were used: bismuth iodide (BiI_3, 99%, Sigma-Aldrich), cesium iodide (CsI, 99.999%, Alfa Aesar GmbH & Co KG, Kandel, Germany), methylammonium iodide (MAI, ≥99%, anhydrous, Sigma-Aldrich), formamidinium iodide (FAI, ≥98%, Sigma-Aldrich), rubidium iodide (RbI, 99.8%, Alfa Aesar GmbH & Co KG, Kandel, Germany), copper iodide (CuI, 99.998%, Alfa Aesar GmbH & Co KG, Kandel, Germany), gold iodide (AuI, >99%, Alfa Aesar GmbH & Co KG, Kandel, Germany), silver iodide (AgI, 99.999%, Alfa Aesar GmbH & Co KG, Kandel, Germany), indium iodide (InI, 99.998%, Alfa Aesar GmbH & Co KG, Kandel, Germany), and other reagents: dimethyl sulfoxide (DMSO, analytical grade, ChemPur, Piekary Slaskie, Poland), dimethylformamide (DMF, analytical grade, POCH S.A., Gliwice, Poland), ethyl acetate (ACS reagent, ≥99.5%, Sigma-Aldrich) oleic acid (OA, technical grade 90%, Sigma-Aldrich), oleylamine (OLAm, ≥98%, Sigma-Aldrich), and toluene (analytical grade, EUROCHEM BGD, Tarnow, Poland). OLAm and OA were dried in a Schlenk line (2 h, 100 °C) before each perovskite synthesis. Toluene was also used to purify perovskites. To prepare the electrolytes used for photocatalytic research, double-deionized water, methanol (CH_3OH, analytical grade, STANLAB, Lublin, Poland), and hydroiodic acid (HI, 57 wt% aqueous solution, distilled, stabilized by 0.75% H_3PO_2, Acros Organics, Geel, Belgium), and hypophosphorus acid (H_3PO_2, 50 wt% aqueous solution, Alfa Aesar GmbH & Co KG, Kandel, Germany) were used. For the photoreduction of platinum onto Cs_2AuBiI_6 sample potassium tetrachloroplatinate (K_2PtCl_4, 99.99%, Alfa Aesar GmbH & Co KG, Kandel, Germany) as a platinum precursor and anhydrous ethanol (C_2H_5OH, 99.8 vol%, POCH S.A., Gliwice, Poland) as reaction medium were used.

The morphologies of the obtained materials were examined using field-emission scanning electron microscopy (FE-SEM, JEOL JSM-7610F). Powder X-ray diffraction experiments were conducted at 20 °C on powdered samples using a Bruker D8 Focus diffractometer with Cu Kα (λ = 1.54 Å) radiation and a LynxEye XE-T detector. Data were collected from 10° to 60° over a scan time of 30 min. LeBail refinement of the powder X-ray diffraction (pXRD) pattern was performed to determine the crystal structure type and lattice parameters of the tested samples, using HighScore Plus ver. 3.0e software. Diffuse reflectance spectra were recorded using a UV–Vis spectrophotometer (UV 2600, Shimadzu) equipped with four integrating sphere in the range of 300–700 nm using $BaSO_4$ as a non-absorbing reference. Photoluminescence (PL) measurements were performed at 20 °C using an LS-50B luminescence spectrophotometer equipped with a Xe discharge lamp as the excitation source and an R928 photomultiplier as the detector. Excitation radiation (λ_{ex} = 330 nm) was directed at the sample surface at an angle of 90°. The surface elemental composition of the photocatalysts was evaluated via X-ray photoelectron spectroscopy (XPS) using a PHI 5000 VersaProbe™ Scanning ESCA Microprobe (ULVAC-PHI, Chigasaki Japan) instrument. High-resolution (HR) XPS spectra were recorded using monochromatic Al Kα radiation (hν = 1486.6 eV) from an X-ray source operating at 100 μm spot size, 25 W, and 15 kV. The analyzer pass energy was 23.5 eV and the energy step size 0.1 eV. The binding energy scale was referenced to the C 1 s peak, with BE = 284.8 eV. The transmission function of the spectrometer was determined to quantify the PHI MultiPak sensitivity factors. The Brunauer–Emmett–Teller (BET) surface areas of the obtained samples were determined using a 3P Instrument Micro 200 sorption analyzer. Each sample was degassed for 5 h at 200 °C before measurement.

2.2. Preparation of $A_3Bi_2I_9$ and $Cs_2B'BiI_6$ samples

Both types of materials, single halide perovskites $A_3Bi_2I_9$ and $Cs_2B'BiI_6$, were synthesized using the ligand-assisted reprecipitation technique (LARP) and the synthesis scheme is shown in Fig. 1.

Briefly, an appropriate amount of AI salts (where A = Cs, Rb, MA, or FA) was dissolved in a DMSO/DMF (1 mL/9 mL) solvent mixture and an appropriate amount of BiI_3 was dissolved in 10 mL of ethyl acetate at room temperature under an ambient atmosphere. Then, the two solutions were mixed and 125 μL of OLAm was added. Meanwhile, an antisolvent was prepared by mixing 200 mL toluene with 25 mL OA under an ambient atmosphere. After 10 min of vigorous magnetic stirring of the precursor solution and antisolvent, the precursor solution was slowly dropped into the antisolvent under continuous stirring for 10 min. Then, the solid product was separated by centrifugation (10 min, 10,000 rpm) and the obtained powder was sequentially washed with toluene four times and centrifuged (10,000 rpm). Finally, the pure product was vacuum dried at 100 °C for 24 h. To form $Cs_2B'BiI_6$, an additional precursor, B'I type (where B′ = Ag, Au, In, Cu), was introduced into the BiI_3 solution in ethyl acetate.

The following perovskite types were obtained in the same manner: $A_3Bi_2I_9$ (where A = Cs, Rb, MA, FA) and $Cs_2B'BiI_6$ (where B′ = Ag, Au, In, Cu). Additionally, OLAm and OA were dried at 100 °C for 2 h in the Schlenk line before use in the aforementioned synthesis of single and double perovskite crystals. Table 1 lists the qualitative and quantitative compositions of the perovskite precursor solutions.

2.3. Cs_2AuBiI_6 modified with Pt

The photodeposition method was used to prepare Cs_2AuBiI_6

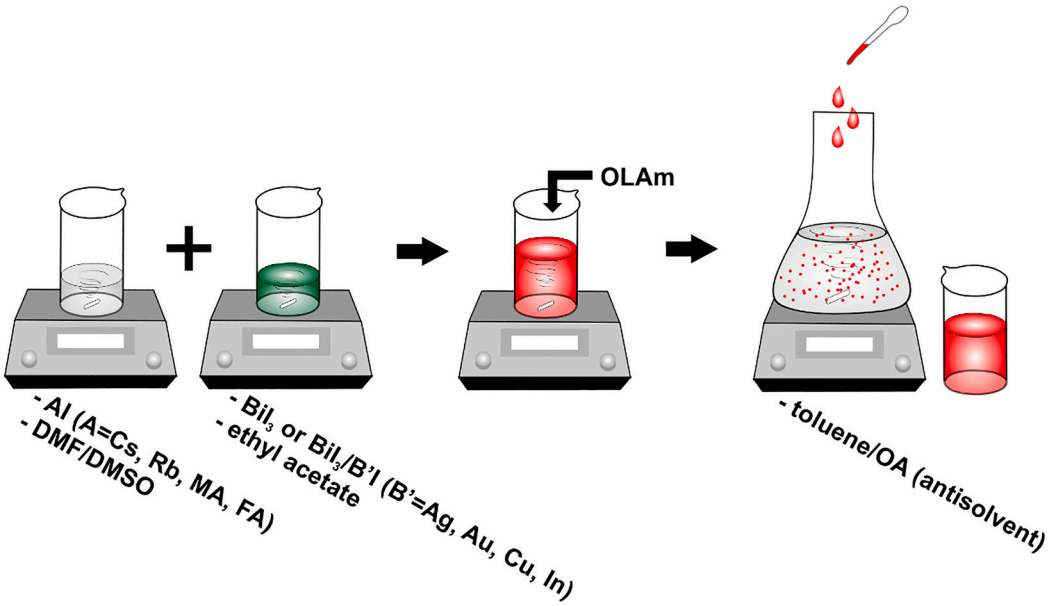

Fig. 1. Scheme of single halide perovskites $A_3Bi_2I_9$ type and $Cs_2B'BiI_6$ sample preparation route via the LARP technique.

Table 1
Obtained $Cs_3Bi_2X_9$ and the type and concentration of precursors used in the synthesis.

Sample label	Type of precursor	Amounts of precursor (mmol)
$Cs_3Bi_2I_9$	CsI	2.00
	BiI_3	1.34
$Rb_3Bi_2I_9$	RbI	2.00
	BiI_3	1.34
$MA_3Bi_2I_9$	MAI	2.00
	BiI_3	1.34
$FA_3Bi_2I_9$	FAI	2.00
	BiI_3	1.34
Cs_2AgBiI_6	CsI	2.00
	AgI	1.00
	BiI_3	1.00
Cs_2AuBiI_6	CsI	2.00
	AuI	1.00
	BiI_3	1.00
Cs_2InBiI_6	CsI	2.00
	InI	1.00
	BiI_3	1.00
Cs_2CuBiI_6	CsI	2.00
	CuI	1.00
	BiI_3	1.00

modified with platinum nanoparticles on the surface (0.5 mol%). An appropriate amount of Cs_2AuBiI_6 powder and a metal precursor aqueous solution were mixed with 20 mL of anhydrous ethanol. The suspension was then transferred to a quartz glass photoreactor with a total volume of 25 mL. The as obtained suspension was stirred in the dark for 0.5 h and the headspace of the reactor was degasified with nitrogen for 1 h. Finally, the reactor was irradiated at 10 °C for 1 h and then, the modified powder was centrifuged (6000 rpm, 10 min) and dried at 60 °C overnight under atmospheric pressure.

2.4. Photocatalytic performance

A cylindrical quartz reactor was charged with the photocatalyst (dose 1.25 g/L) and one type of aqueous electrolyte simultaneously and then tightly closed with a silicone septum. The suspension was stirred at 700 rpm and a constant temperature of 10 °C. For the first 0.5 h, the process was run without irradiation to establish an adsorption-desorption equilibrium between the photocatalyst and the solution, and the headspace was purged with nitrogen. Then, a reference gaseous sample was collected using a syringe and analyzed. The system was subsequently irradiated by a 1000-W Xe lamp (Oriel), and control samples were collected every hour. The total irradiation time was 4 h and the hydrogen content of the collected air samples was determined using a gas chromatograph equipped with a Thermal Conductivity Detector. To compare the stability of the perovskites during photocatalytic performance, two different electrolytes were used. The first electrolyte, which was established using 10 vol% MeOH aqueous solution and the second electrolyte was formed by creating a HI/H_3PO_2 (*v*/v; 4/1) saturated solution of an individual perovskite and then filtrated thought syringe filter. Both electrolytes were used as reaction media to check the photoactivity and stability of single perovskite $Cs_3Bi_2I_9$ under UV–Vis light. Because of the weak stability of the halide perovskite structure in aqueous methanolic solution, the most active single perovskite $Cs_3Bi_2I_9$ was also tested under visible light (a long-pass filter with a cut-off of 420 nm was employed) in the HI/H_3PO_2 electrolyte. To achieve even higher photoactivity under visible light, we attempted to experimentally create double perovskites with A–cations as Cs (Cs_2AgBiI_6, Cs_2AuBiI_6, Cs_2InBiI_6, Cs_2CuBiI_6) and determine their activity under visible light irradiation in a HI/H_3PO_2 electrolyte in the same manner as above.

The most active sample, Cs_2AuBiI_6/0.5% Pt, was also tested in a long-term stability test under visible light (>420 nm) in HI/H_3PO_2 electrolyte for 16 h, with gaseous samples collected every 1 h and immediately analyzed using GC/TCD.

3. Results and discussion

3.1. Morphology

Comprehensive SEM microscopic analysis of the obtained photocatalysts was performed to reveal the characteristic morphological features and differences between the samples. Fig. 2 shows the SEM images of all synthesized single perovskites $A_3Bi_2I_9$ type, where A – Cs (Fig. 2 a-c), Rb (Fig. 2 d-f), MA (Fig. 2 g), and FA (Fig. 2 h). In the case of morphology, the most regular shape of the particles was formed by the $Cs_3Bi_2I_9$ perovskite. Fig. 2 a-c shows flattened hexagonal prisms of different sizes, characteristic of this compound [50,51]. However, $Rb_3Bi_2I_9$ particles (Fig. 2 d-f) formed irregular aggregated shapes with characteristic sharp elements. The SEM images of $MA_3BI_2I_9$ and $FA_3Bi_2I_9$ (Fig. 1 g and h, respectively) show irregular structures of aggregated

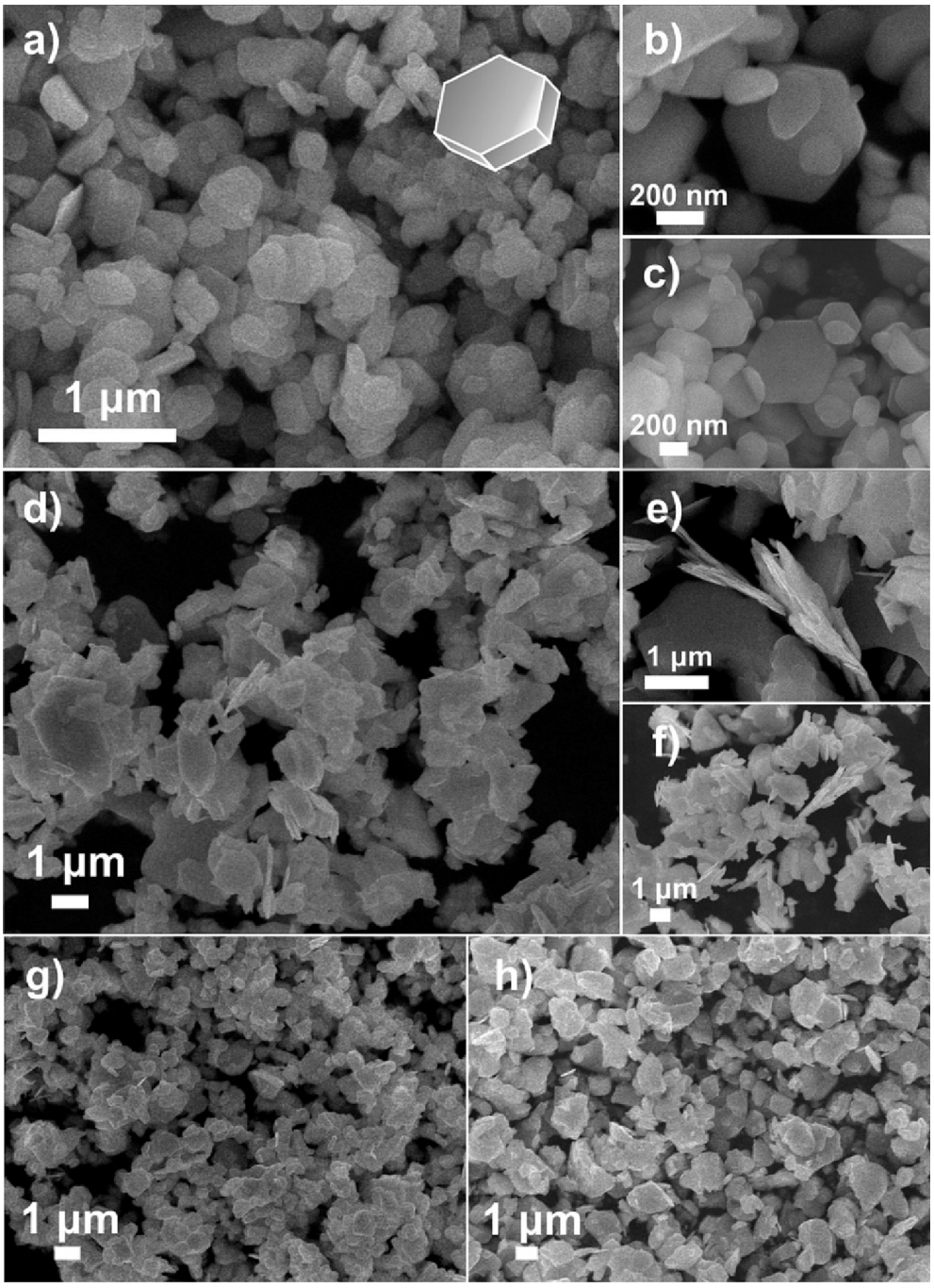

Fig. 2. SEM images of single perovskites: (a-c) $Cs_3Bi_2I_9$, (d-f) $Rb_3Bi_2I_9$, g) $MA_3Bi_2I_9$ and h) $FA_3Bi_2I_9$.

particles. Thus, the SEM images of single perovskites revealed differences in morphology according to the change in the A-cation in the $A_3Bi_2I_9$ general formula.

Fig. 3 shows the SEM images of Cs_2AgBiI_6 (a, b), Cs_2AuBiI_6 (c, d), Cs_2InBiI_6 (e), and Cs_2CuBiI_6 (f). The introduction of an additional cation source ($B' = Ag^+$, Au^+, In^+ or Cu^+) into the synthesis of $Cs_3Bi_2I_9$ caused significant changes in morphology. No samples showed visible hexagonal particles; however, for modification by Ag cations (Cs_2AgBiI_6), microrods with sticky fine particles formed (Fig. 3 a, b). No characteristic morphological features were identified for the remaining samples: Cs_2AuBiI_6, Cs_2InBiI_6, and Cs_2CuBiI_6. The structures shown in Fig. 3 (c-f) are similar; the observed particles are different in size, irregular in shape, and aggregated. The observed aggregation of particles also resulted in a decrease in the specific surface area (Table S1 in Supporting Information).

3.2. XRD

Fig. 4 presents the powder X-ray diffraction (pXRD) patterns of the $A_3Bi_2I_9$ type samples, where A = Cs, Rb, MA, and FA. The red solid line in Fig. 4 is the profile fit (LeBail) and the green vertical marks show the expected Bragg reflections for each model. The refined lattice parameters are listed in Table 2 and are in agreement with those reported in the literature for $Cs_3Bi_2I_9$ [48], $Rb_3Bi_2I_9$ [52], $MA_3Bi_2I_9$ [53], and $FA_3Bi_2I_9$ [54], confirming successful synthesis.

Notably, $Cs_3Bi_2I_9$, $MA_3Bi_2I_9$, and $FA_3Bi_2I_9$ samples formed in the same hexagonal crystal structure (P63/mmc), except for $Rb_3Bi_2I_9$ which formed in monoclinic (P21/c).

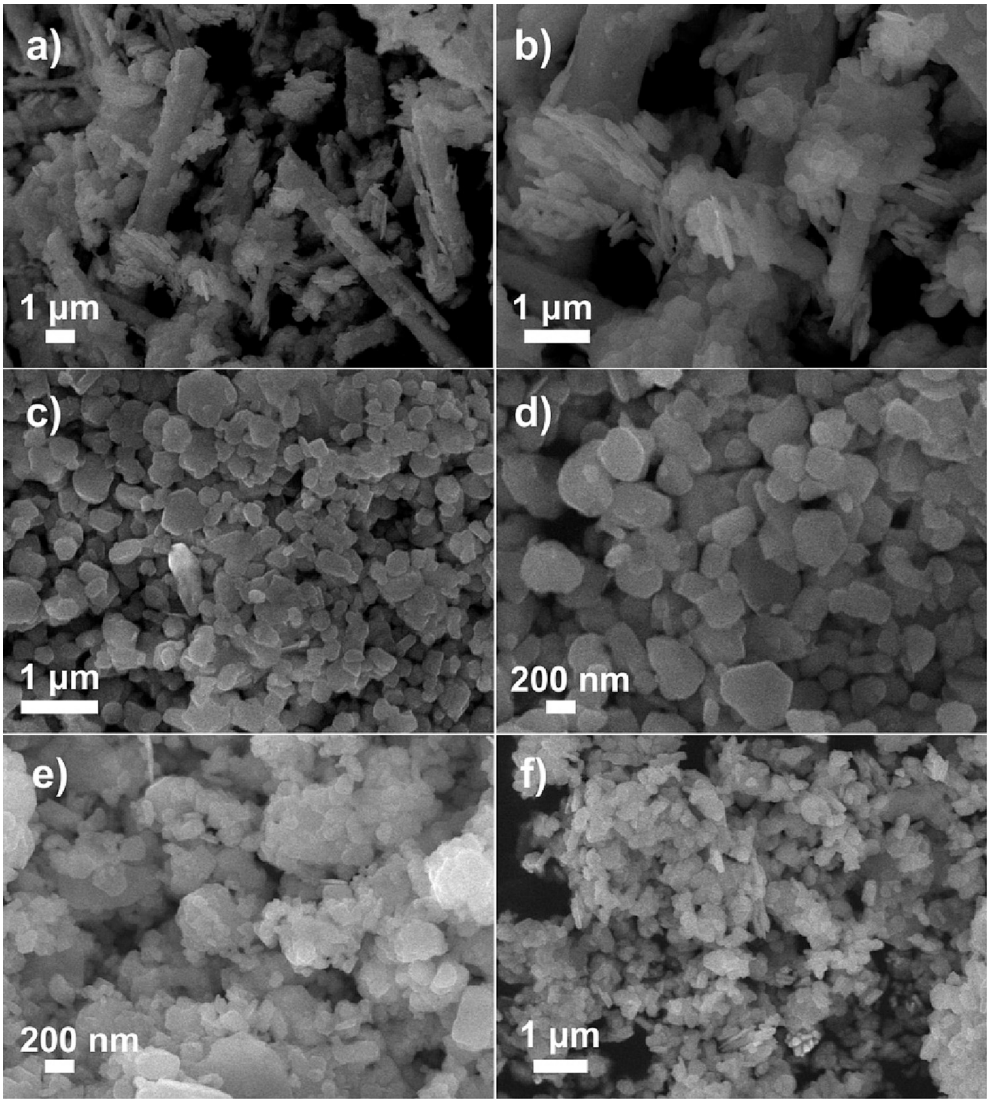

Fig. 3. SEM images of (a, b) Cs_2AgBiI_6, (c, d) Cs_2AuBiI_6, e) Cs_2InBiI_6 and f) Cs_2CuBiI_6.

For the most photoactive sample, $Cs_3Bi_2I_9$, for the first time, we attempted to introduce metallic cations (Ag, Au, In, Cu) into the structure to form a double perovskite. The series of patterns shown in Fig. 5 presents the pXRD data for the samples labeled Cs_2AgBiI_6, Cs_2AuBiI_6, Cs_2InBiI_6, and Cs_2CuBiI_6.

In the case of the above four samples, we recognized reflections characterized by the $Cs_3Bi_2I_9$ hexagonal phase as the dominant phase, and an additional crystal phase for each. None of these indicated the presence of a double iodo-perovskite structure. The samples labeled Cs_2AgBiI_6 and Cs_2CuBiI_6 additional crystalline phases indicate the presence of $CsAg_2I_3$ [55] and $CsCu_2I_3$, respectively. The XRD pattern of Cs_2AuBiI_6 confirmed the presence of an Cs_3IO additional phase and the pattern of Cs_2InBiI_6 revealed reflections corresponding to the presence of a small quantity of CsI crystals as the synthesis residue. Unfortunately, the results obtained for Cs_2AuBiI_6 and Cs_2InBiI_6 did not confirm the presence of Au-and In-based compounds. This phenomenon can be observed in the appearance of metallic species of gold and indium over these photocatalysts (see XPS results, Fig. 7).

Additionally, for the most photoactive single perovskite under both UV–Vis and Vis light in 10% MeOH and HI/H_3PO_2 electrolytes, XRD and SEM analyses were performed for the powder after photocatalytic performance to determine the influence of each type of electrolyte on the stability of the perovskites. The results are detailed in SI (see Fig. S1).

3.3. Optical properties

To analyze the optical properties of the obtained materials, the absorption and emission spectra were measured in the ranges of 300–700 and 300–800 nm, respectively. All recorded absorption and emission spectra are presented in Figs. 6 a and b. Each of the prepared photocatalysts exhibited absorption bands nearly in the same region up to approximately 600 nm and each had a characteristic peak corresponding to the $n = 1$ excitonic transition (at around 483–486 nm; with one exception at 467 nm for the weak transition peak belonging to the $Rb_3Bi_2I_9$ absorption band). This phenomenon is characteristic of bismuth-based iodo-perovskite structures [48,56,57]. Based on the measured absorption spectra, the energy BGs of all pristine in-phase samples were calculated according to Eq. (1):

$$[F(R)h\nu]n = A(h\nu - Eg) \quad (1)$$

where $h\nu$ is the photon energy, A is the proportionality constant, Eg is the width of the BG, $n = 2$ for a direct transition or 1/2 for an indirect transition, and F(R) is the Kubelka–Munk function. The obtained results are presented in Fig. 6 c–d. The BGs widths were estimated by extrapolating the linear region. Such an analysis was performed only for pristine semiconductors [38]; thus, according to the XRD results (Figs. 4 and 5), the Kubelka–Munk function was designated only for $Cs_3Bi_2I_9$,

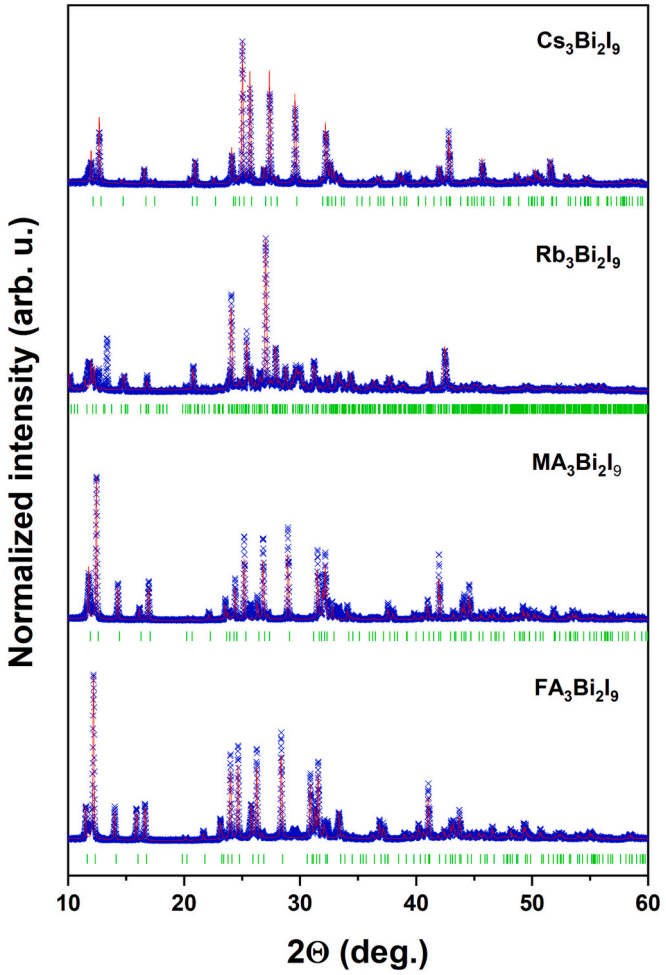

Fig. 4. Powder x-ray diffraction patterns for $A_3Bi_2I_9$ (where A = Cs, Rb, MA, and FA) samples. Experimental data are shown by blue x's symbols. The calculated profile and expected Bragg reflections are represented by a red line and green vertical ticks. (For interpretation of the references to colour in this figure legend, the reader is referred to the web version of this article.)

Table 2
Refined lattice parameters for $Cs_3Bi_2Cl_9$, $Rb_3Bi_2Br_9$, $MA_3Bi_2I_9$, and $FA_3Bi_2I_9$ samples.

Sample label	a (Å)	b (Å)	c (Å)	β (°)	Crystal structure
$Cs_3Bi_2I_9$	8.4169 (2)	–	21.205 (1)	–	Hex. s.g. P63/mmc (#194)
$Rb_3Bi_2I_9$	14.611 (1)	8.1720 (6)	20.917 (2)	91.6	Mono. s.g. P21/c (#14)
$MA_3Bi_2I_9$	8.5770 (2)	–	21.744 (1)	–	Hex. s.g. P63/mmc (#194)
$FA_3Bi_2I_9$	8.7631 (2)	–	22.113 (1)	–	Hex. s.g. P63/mmc (#194)

$Rb_3Bi_2I_9$, $MA_3Bi_2I_9$, and $FA_3Bi_2I_9$. Moreover, the geometric mean total Mulliken's absolute electronegativity for each pristine perovskite was calculated and then it was possible to determine the edge potentials of the valence and conduction bands (using Butler and Ginley's relationship). The calculations of the CB and VB using this method are presented in detail in the SI and the data obtained are presented in Table 3. All the samples exhibited narrowband characteristics and the widths of their BGs were similar. This finding means that the band gap width of the same group of Bi-based halide perovskites strictly depends on the type of halogen, less than cation A. Moreover, the calculated direct BGs for each

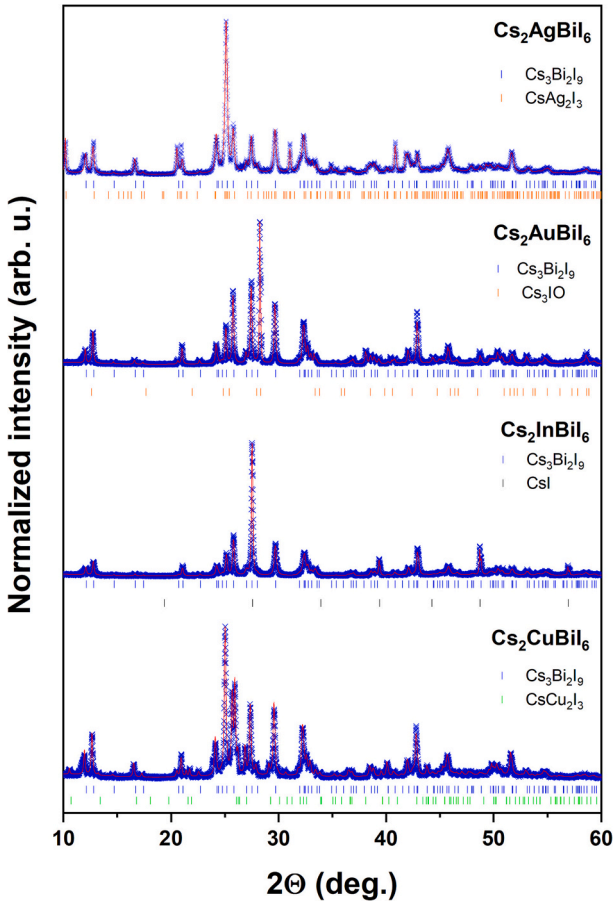

Fig. 5. Powder X-ray diffraction patterns for Cs_2AgBiI_6, Cs_2AuBiI_6, Cs_2InBiI_6, and Cs_2CuBiI_6 samples. Experimental data are shown by blue x's symbols. The calculated profile and expected Bragg reflections of all identified phases are represented by a red line and different colour vertical ticks depends on phase. (For interpretation of the references to colour in this figure legend, the reader is referred to the web version of this article.)

pristine perovskite were slightly higher than those of the indirect analog.

The literature indicates that Bi-based halide perovskites are mainly endowed with an indirect BG because of the gap in proving the existence of a direct BG [56,57] but it is possible to identify the specific direct nature of electronic transitions in $Cs_3Bi_2X_9$ perovskites [48,58]. In this work, to improve the double-fold nature of Bi-based perovskite BGs and to characterize their luminescence features, PL spectra were recorded and are shown in Fig. 6 b. It is clear that the PL profiles for each sample exhibit two different maxima of luminescence, which are affected by the recombination process. The slightly higher PL band at approximately 380 nm corresponds to the intermediate electron transition and the second band at approximately 660 nm and lower intensity (affected by longer relaxation time) indicated a direct excitonic transition. Therefore, we proved that the BG values of the obtained samples were two-fold. In addition, in the recorded spectra, the highest luminescence ability was observed for $MA_3Bi_2I_9$, in contrast to Cs_2InBiI_6, whose luminescence intensity was negligible.

3.4. XPS

The elemental composition in the surface region of both types of materials, $A_3Bi_2I_9$ (A = Cs, Rb, MA, FA) and $Cs_2B'BiI_6$ (B′ = Ag, Au, In, Cu), was evaluated via XPS (see Table 4).

Fig. 7 shows the high-resolution (HR) XPS spectra of the elements detected in the single perovskites. The chemical characteristics of the elements are shown in Fig. 7. The Cs 3d [48,59], Rb3d [59,60], Bi 4f

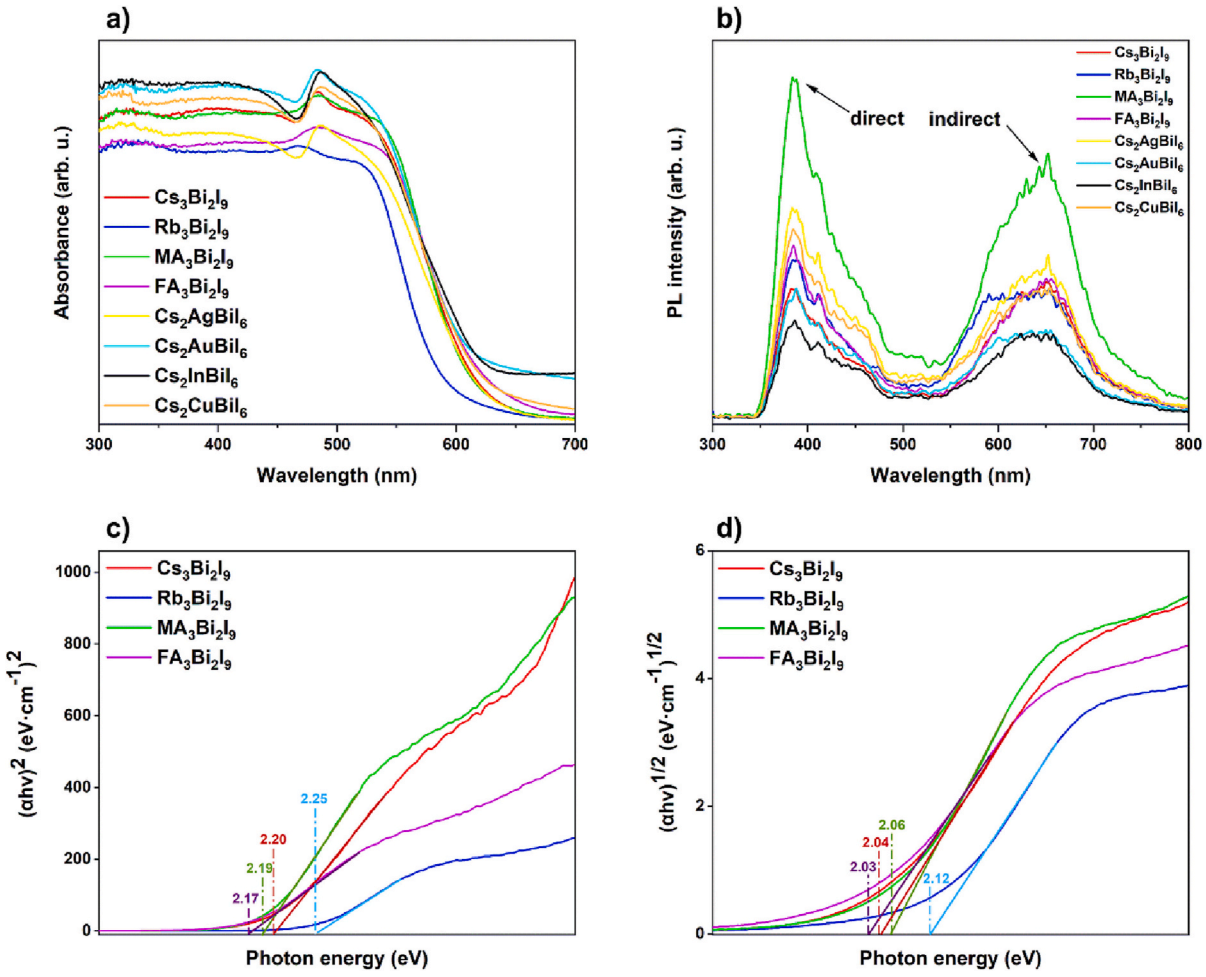

Fig. 6. a) UV–Vis/diffuse reflectance spectra; b) PL spectra (λ_{ex} = 330 nm) of all obtained photocatalysts; c,d) transformed Kubelka–Munk (from diffuse reflectance spectra) function vs. photon energy determining the direct (c) and indirect (d) band gap width of pristine perovskites ($Cs_3Bi_2I_9$, $Rb_3Bi_2I_9$, $MA_3Bi_2I_9$ and $FA_3Bi_2I_9$).

Table 3
Calculated values of direct and indirect band gap widths and edges potentials of conduction and valence bands of the prepared semiconductors.

Semiconductor	Width of indirect band gap (eV)	Width of direct band gap (eV)	Edge of a CB based on the indirect band gap (V)	Edge of a VB based on the indirect band gap (V)	Edge of a CB based on the direct band gap (V)	Edge of a VB based on the direct band gap (V)
$Cs_3Bi_2I_9$	2.04	2.20	−0.58	1.46	−0.66	1.54
$Rb_3Bi_2I_9$	2.12	2.25	−0.55	1.57	−0.61	1.64
$MA_3Bi_2I_9$	2.06	2.19	1.24	3.30	1.17	3.36
$FA_3Bi_2I_9$	2.03	2.17	1.26	3.29	1.19	3.36

Table 4
Elemental contents in the surface layer of $A_3Bi_2I_9$ (A = Cs, Rb, MA, FA) and Cs_2MBiI_6 (M = Ag, Au, In, Cu) samples evaluated by XPS.

	Elemental composition (atomic%.)												Atomic ratios		
Sample label	Cs	Bi	I	C	O	Rb	N	Ag	Au	In	Cu	Pt	A/Bi	M/Bi	I/Bi
$Cs_3Bi_2I_9$	3.27	3.36	7.78	80.41	5.18	0	0	0	0	0	0	0	0.97	–	2.32
$Rb_3Bi_2I_9$	0	18.24	17.56	44.59	7.42	12.19	0	0	0	0	0	0	0.67	–	0.96
$MA_3Bi_2I_9$ *	0	17.45	18.67	50.69	5.50	0	7.69	0	0	0	0	0	0.44	–	1.07
$FA_3Bi_2I_9$ **	0	11.40	17.41	52.91	7.13	0	11.15	0	0	0	0	0	0.98	–	1.53
Cs_2AgBiI_6	5.88	6.22	15.81	66.04	4.93	0	0	1.12	0	0	0	0	–	0.180	2.54
Cs_2AuBiI_6	5.03	6.50	13.05	70.69	4.42	0	0	0	0.31	0	0	0	–	0.048	2.01
Cs_2InBiI_6	5.52	11.53	14.35	62.83	5.48	0	0	0	0	0.30	0	0	–	0.026	1.24
Cs_2CuBiI_6	1.16	1.41	3.14	91.14	2.44	0	0	0	0	0	0.71	0	–	0.504	2.23
Cs_2AuBiI_6 / 0.5% Pt	8.84	19.16	23.30	40.53	7.62	0	0	0	0.34	0	0	0.22	–	0.018	1.22

* MA = methylammonium cation.
** FA = formamidinium cation.

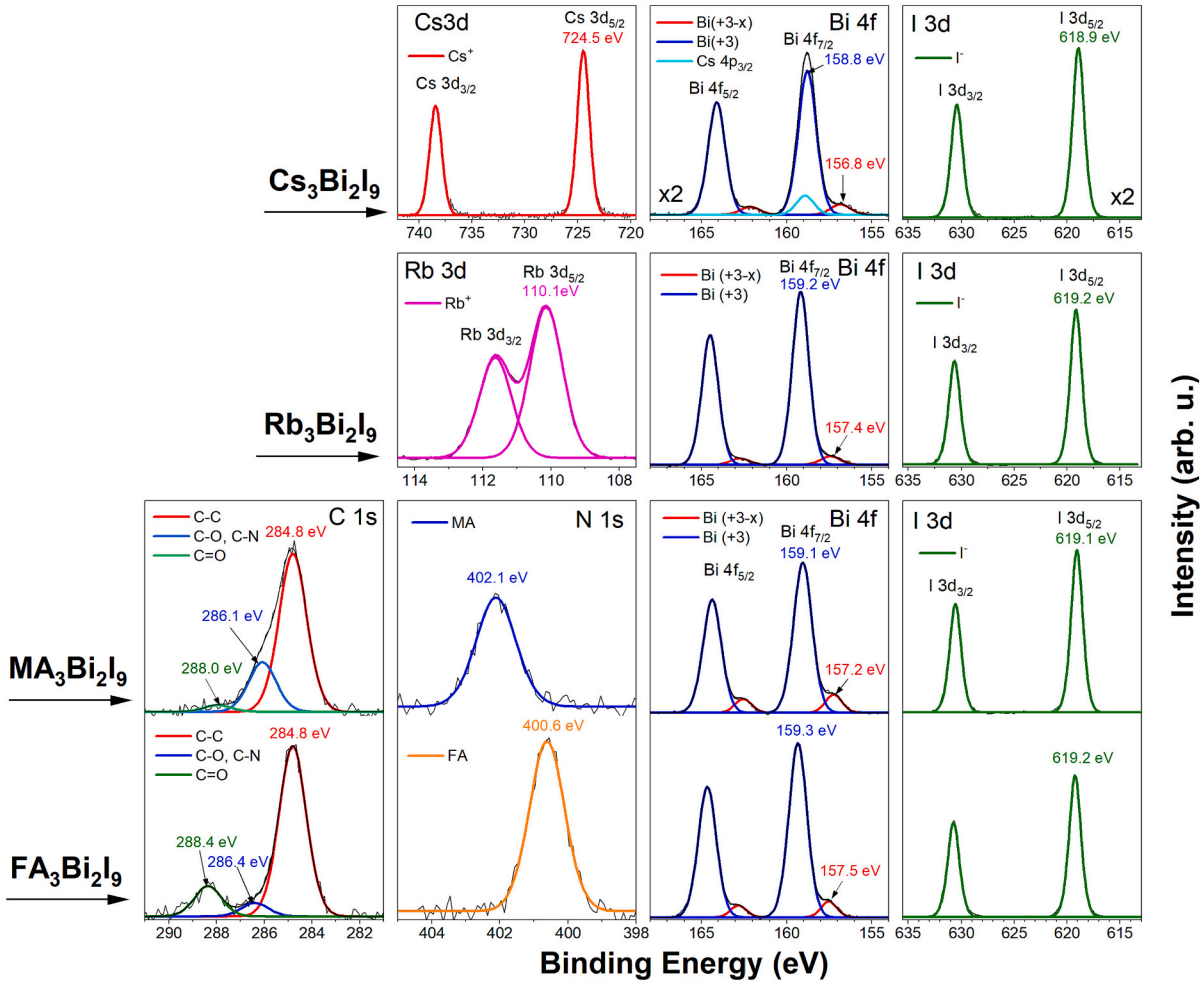

Fig. 7. High resolution Cs 3d, Bi4f, I 3d, C 1 s and N 1 s spectra recorded on the single perovskites $A_3Bi_2I_9$ (A = Cs, Rb, MA, FA).

[48,59], and I 3d [48,59] spectra identified Cs, Rb, Bi, and I in the $Cs_3Bi_2I_9$ and $Rb_3Bi_2I_9$ samples. The C 1 s and N 1 s spectra confirmed the successful synthesis of $MA_3Bi_2I_9$ and $FA_3Bi_2I_9$ perovskites using MA and FA cations. The C1s and N 1 s signals located at BE of 286.1 and 402.1 eV, respectively, agree well with the corresponding data reported for other perovskites with methylamine [61,62]. In contrast, the relatively large contribution of the C—N fraction in the C 1 s spectrum (BE of 288.4 eV) and the position of the N 1 s peak (BE of 400.6 eV) attest to the synthesis of the $FA_3Bi_2I_9$ sample involving the formamidinium cation [63].

Fig. 8 presents the HR spectra of the metallic cations (Ag, Au, In, Cu, and Pt) used to form $Cs_2B'BiI_6$ samples and for the modification of Cs_2AuBiI_6 by Pt. The Ag 3d spectrum (a) confirms the presence of Ag^{+1} [59] in the surface area of Cs_2AgBiI_6. The Au 4f spectrum of Cs_2AgBiI_6 (b) reveals two chemical states of Au, formed by $4f_{7/2}$ and $4f_{5/2}$ spin-orbit splitting components, with an intensity ratio of 4:3 and separated by 3.67 eV. The first state, at the BE of $Au4f_{7/2}$ close to 83.7 eV, is attributed to Au^{+1} and the second state ($Au4f_{7/2}$ at 85.8 eV) to Au^{+3} components [64]. The In 3d spectrum of Cs_2InBiI_6 (c) overlaps with the Bi $4d_{5/2}$ signal, but after deconvolution, it indicates the presence of In^{3+} surface species [59]. The Cu 2p spectrum of the Cs_2CuBiI_6 (d) coincides with Bi 4 s, In $3p_{1/2}$, and Cs MNN signals. After deconvolution, we identified the Cu 2p spectral features characteristic of the Cu^{1+} species [65]. To identify the Pt in the most active sample, Cs_2AuBiI_6/0.5% Pt, we analyzed the Pt 4d spectrum (e). The Pt $4d_{5/2}$ signal positioned at 317.0 eV confirmed the presence of Pt^{2+} surface species [59].

The inspection of the XPS data in Table 4 clearly shows that the atomic ratios A/Bi and B′/Bi, which are related to the obtained materials $A_3Bi_2I_9$ (A = Cs, Rb, MA, FA) and $Cs_2B'BiI_6$ (B′ = Ag, Au, In, Cu), respectively, are much lower than the corresponding stoichiometric ratios for $A_3Bi_2I_9$ and $Cs_2B'BiI_6$ (A/Bi = 1.5 and B′/Bi = 1). Moreover, the I/Bi atomic ratios for all samples were much lower than the corresponding stoichiometric ratios for $A_3Bi_2I_9$ and $Cs_2B'BiI_6$ (I/Bi = 4.5 and 6, respectively). This indicates a higher surface concentration of other Bi species, probably BiO_x or $In(OH)_x$.

3.5. Photocatalytic activity

The photoactivity of all the obtained samples was estimated according to the photocatalytic generation of hydrogen molecules under UV–Vis and Vis irradiation. In the first step, single perovskites $A_3Bi_2I_9$ type (where A = Cs, Rb, MA, FA) were tested under UV–Vis light in two different electrolytes, aqueous methanolic solution and HI/H_3PO_2 electrolyte. The obtained results are shown in Fig. 9 a, b, respectively. In both cases, we observed the same relationship in activity, independent of the electrolyte, in the following order: $Cs_3Bi_2I_9$ > $Rb_3Bi_2I_9$ > $MA_3Bi_2I_9$ > $FA_3Bi_2I_9$. Thus, in both cases the highest activity was exhibited by $Cs_3Bi_2I_9$ perovskite. After 4 h of irradiation, around 35.5 μmol/$g_{cat.}$ and 2304 μmol/$g_{cat.}$ was obtained in the reaction over the $Cs_3Bi_2I_9$ photocatalyst under UV–Vis light in 10% MeOH and HI/H_3PO_2 electrolytes, respectively. There was also higher photolysis to form H_2 molecules in the absence of a photocatalyst for the acidic electrolyte (0.6 μmol/$g_{cat.}$) compared with the methanolic solution (0.008 μmol/$g_{cat.}$) after 4 h of irradiation. In addition, each of the single perovskites

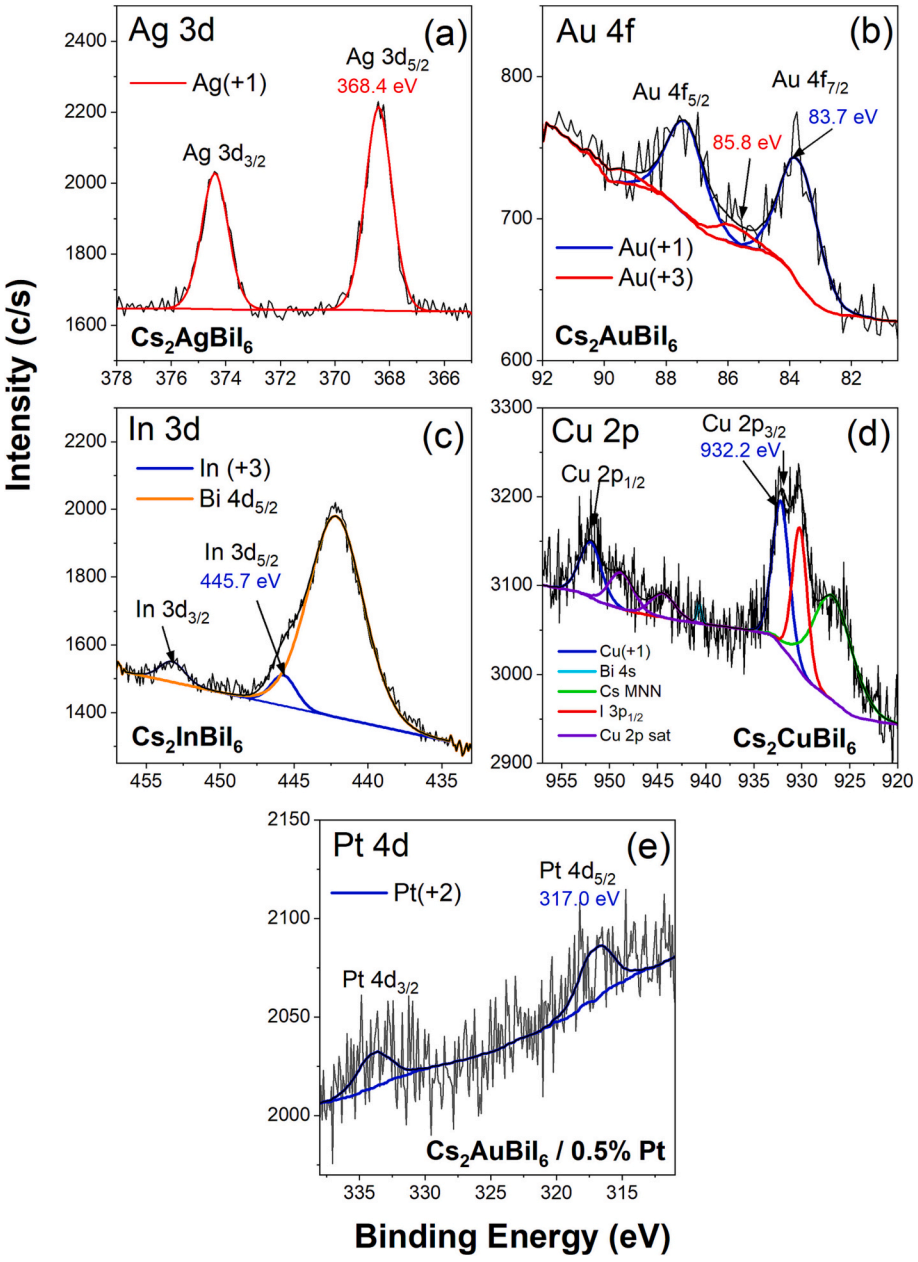

Fig. 8. XPS High resolution Ag 3d (a), Au 4f (b), In 2d (c) and Cu 2p spectra recorded on the double perovskites $A_3Bi_2I_9$ (A = Cs, Rb, MA, FA). Below the Pt 4d (e) spectrum recorded on the Cs_2AuBiI_6/0.5% Pt sample is presented.

was tested in the same reaction in both electrolytes under visible light using a cut-off optical filter (>420 nm). None of the samples showed photoactivity under visible-light irradiation in the 10% MeOH electrolyte, and the process with only $Cs_3Bi_2I_9$ perovskite in the HI/H_3PO_2 electrolyte achieved 10.5 μmol/g_{cat}. Furthermore, no photolysis of either electrolyte was observed in the visible light field.

Thus, to estimate the stability of the $Cs_3Bi_2I_9$ sample during the process in each electrolyte, the powder after reaction under UV–Vis in two different electrolytes was centrifuged, dried, and re-examined by XRD and SEM analyses. The results are presented in SI (see Fig. S1) and demonstrated that the almost 36 times higher activity of the $Cs_3Bi_2I_9$ sample in the HI/H_3PO_2 electrolyte compared to the methanolic solution was affected, among other things, by its increased stability in this environment.

To achieve even higher activity under visible light over the $Cs_3Bi_2I_9$ sample, an attempt was made to obtain novel double perovskite structures by introducing an admixture of a foreign cation (Ag, Au, In, or Cu) at the synthesis stage. These chemical elements were chosen based on literature reports, which were mainly theoretical studies on the possibility of the existence of perovskite connections and their thermodynamic stability [44–47]. Thus, the introduction of foreign ions should create additional electron states, thereby increasing the light absorption capacity and mobility of photoinduced charges while promoting the inhibition of the recombination process. Furthermore, noble metals such as gold or silver can create a surface plasmon resonance (SPR) effect [66–68], collecting electrons on the surface of the photocatalyst which are responsible for reducing the release of hydrogen during the photocatalytic process. The choice of indium can also be justified by its relatively low price, multiple oxidation states (In^0, In^{+1}, In^{+3}), low toxicity, and higher trapping and mobility of electrons [69,70]. Copper, similar to indium, can occur during the photocatalytic reaction in three different oxidation states (Cu^0, Cu^{+1}, Cu^{+2}). However, past reports have shown that Cu^{1+} and mixed Cu^{1+}/Cu^0 cause defects, such as oxygen vacancies, which promote reduction reactions. Moreover, these pairs

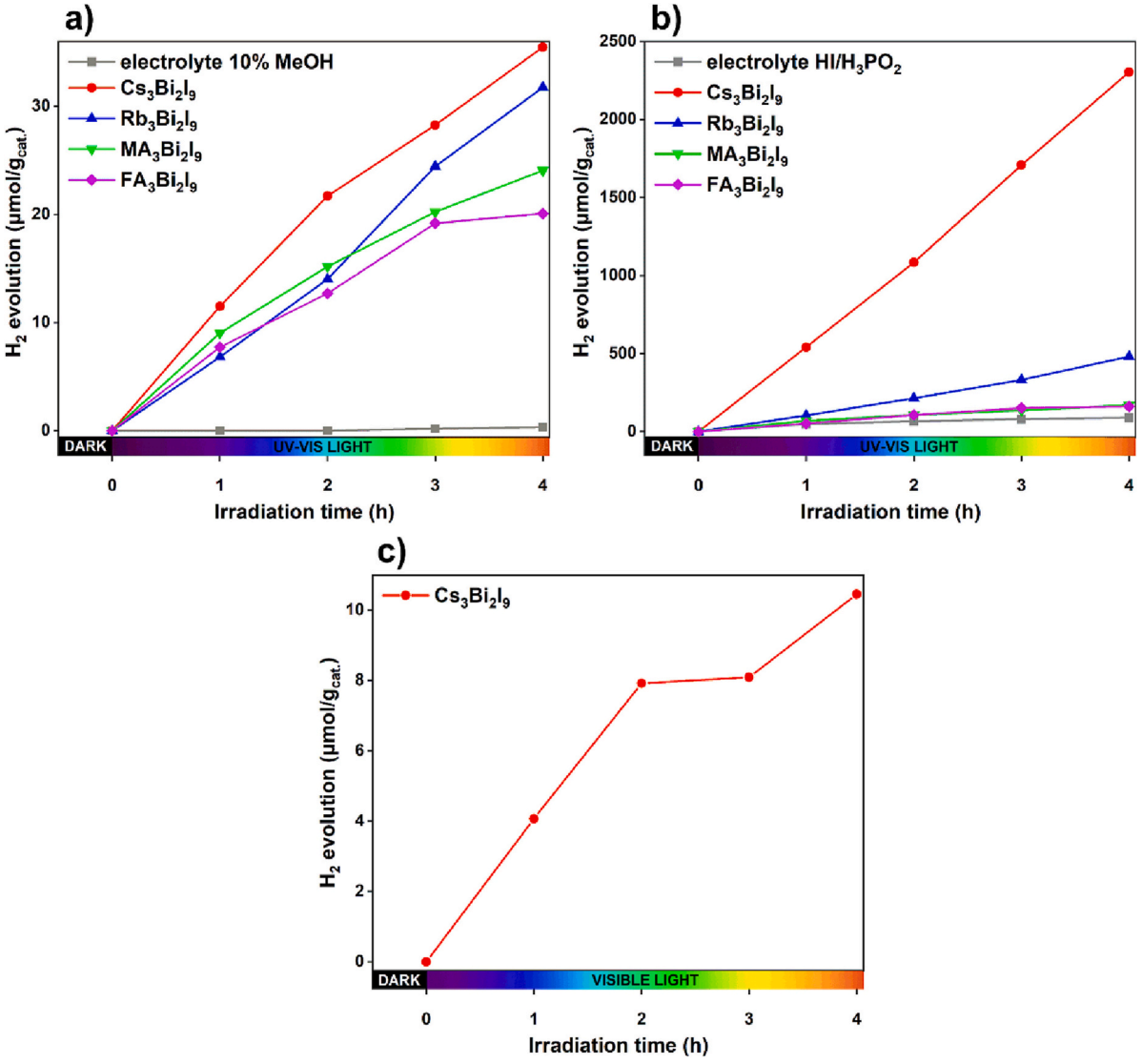

Fig. 9. Photocatalytic hydrogen evolution a) under UV–Vis light with the presence of $A_3Bi_2I_9$ perovskites in 10% MeOH electrolyte; b) under UV–Vis light with the presence of $A_3Bi_2I_9$ perovskites in HI/H_3PO_2 electrolyte and c) efficiency of the process under Vis light (>420 nm) with the presence of $Cs_3Bi_2I_9$ in HI/H_3PO_2 electrolyte.

facilitate the capture and trapping of electrons and holes in various locations [71,72].

Thus, according to our procedure, the as-obtained samples were examined under visible light in a HI/H_3PO_2 electrolyte and the results of photoactivity are shown in Fig. 10 a. The highest activity was achieved by Cs_2AuBiI_6 (84.5 μmol/$g_{cat.}$) and the lowest by Cs_2InBiI_6, which exhibited negligible activity (4.3 μmol/$g_{cat.}$). Then, Cs_2AuBiI_6 photocatalysts were modified with 0.5% Pt and tested again in a prolonged process from 4 to 16 h of irradiation. The obtained results are shown in Fig. 10 b. Modification of Cs_2AuBiI_6 by platinum caused an increase in activity from 84.5 to 105.4 μmol/$g_{cat.}$ after 4 h and 222.3 μmol/$g_{cat.}$ after 16 h of visible light irradiation.

According to the XRD results (Fig. 5), the increase in the photoactivity of the Cs_2AuBiI_6 sample was probably related to the formation of a composite consisting of $Cs_3Bi_2I_9$ and Cs_3IO.

3.6. Mechanism of photocatalytic reaction

None of the double perovskite structures were successfully obtained; therefore, the mechanism of photocatalytic reaction for $Cs_3Bi_2I_9$ single perovskite (in two different electrolytes) was proposed and shown in Fig. 11. During photocatalytic experiments over $Cs_3Bi_2I_9$ perovskite, as a narrowband semiconductor (BG ~ 2.04 eV), it can be photoexcited in the field of visible light and generate e^--h^+ pairs. The photogenerated electrons were transported to the CB of this semiconductor about redox potential value around −0.58 V, and thus the reduction reactions were possible to generate hydrogen molecules. In the first case, a methanolic aqueous solution was used as the reaction medium and the proposed mechanism of the process is illustrated in Fig. 11 a. Methanol plays a key role in preventing the oxidation of holes in the VB of $Cs_3Bi_2I_9$, which normally leads to the oxidation of water molecules to produce oxygen. However, oxygen molecules can react with hydrogen, thereby reversing this reaction. MeOH in the reaction medium reacts with the holes to form oxidized products such as formic acid, formaldehyde, carbon oxides, and even hydrogen gas [73,74]. This reaction is called methanol photoreforming [73]. By examining the powder after the reaction, we proved that the oxidation of the iodo-based perovskite photocatalyst to form the BiOI structure also takes place in this environment (see Fig. S1).

In the second case, hydroiodic acid with hypophosphorus acid (as the stabilizer) was used as the medium for the photocatalytic process (see Fig. 11 b). The oxidizing effect of the holes was used to oxidize iodide (I^-) to triiodide anions (I_3^-), which can be consumed by H_3PO_2

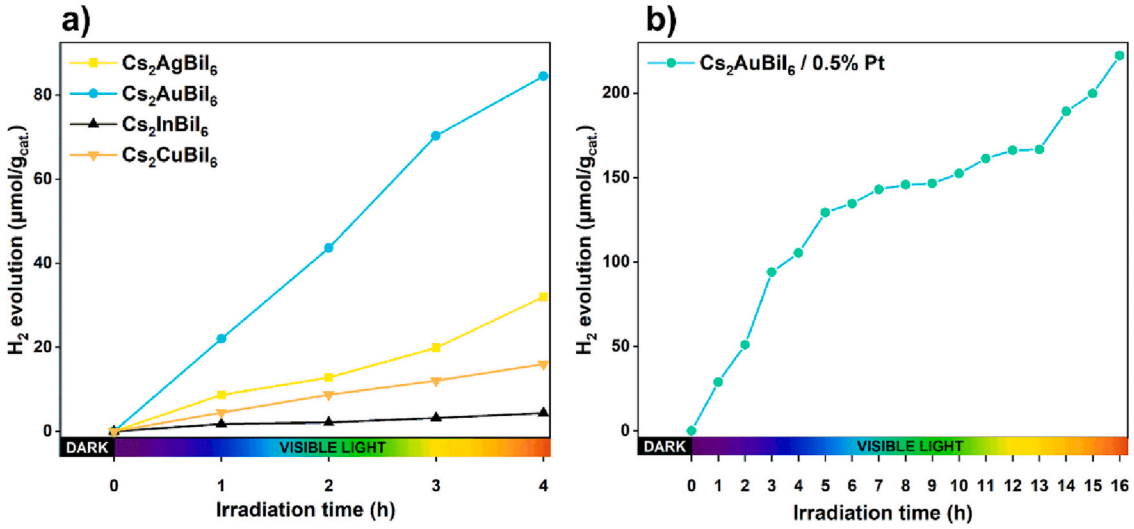

Fig. 10. Photocatalytic hydrogen evolution a) under Vis light (>420 nm) with the presence of $Cs_2B'BiI_6$ photocatalysts (where B′ = Ag, Au, In or Cu) in HI/H_3PO_2 electrolyte, and b) under Vis light (>420 nm) with the presence of Cs_2AuBiI_6 modified with 0.5% Pt in HI/H_3PO_2 electrolyte in prolonging up to 16 h process.

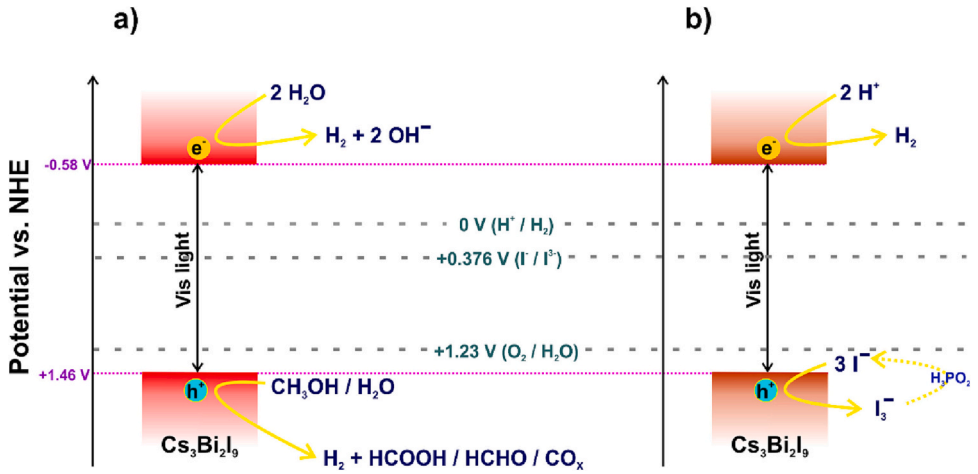

Fig. 11. Schematic illustration of the photocatalytic performance to hydrogen evolution over $Cs_3Bi_2I_9$ photocatalyst under visible light (λ > 420 nm) irradiation in two different electrolytes a) 10% MeOH and b) HI/H_3PO_2 solution.

[25,29,75]. The application of this approach allows for the effective separation of photogenerated charges and thus the achievement of higher process efficiency with the use of the same photocatalyst. Moreover, the electrolyte used increased the stability of the $Cs_3Bi_2I_9$ photocatalyst (Fig. S1).

However, the photocatalytic mechanism in two different electrolytes was presented for a single halide perovskite $Cs_3Bi_2I_9$ because the sample that showed the highest activity was difficult to identify (sample label Cs_2AuBiI_6). Based on the results of the XRD analysis, two crystalline phases were identified: the dominant phase from the $Cs_3Bi_2I_9$ single perovskite and a small contribution from the Cs_3IO phase. In contrast, XPS identified the cations of gold in the +1 and + 3 states of oxidation. Thus, the phenomenon of the highest activity is probably due to the combination of two crystalline phases, $Cs_3Bi_2I_9$ and Cs_3IO, as well as the presence of gold ions on the surface, which in the course of irradiation can be reduced to metallic gold, showing SPR [66–68]. Moreover, the connection of the two semiconductors enables the transport of photogenerated charges between them, thus inhibiting the recombination process. However, the mechanism for the sample Cs_2AuBiI_6 has not been presented in this scheme because the potential of the valence and conduction bands for one of the components, Cs_3IO, is not known. Hence, it is conjectured that Cs_3IO (similar to other compounds in this group: alkali-metal halide oxides M_3XO (M = K, Rb, Cs; X = Cl, Br, I) [76]) belongs to narrow-band semiconductors and, combined with $Cs_3Bi_2I_9$, both can be excited by the energy of the visible region.

4. Conclusion

In this work, we successfully obtained four single Bi-based iodo-perovskites with different A cations ($A_3Bi_2I_9$ where A means Cs, Rb, MA and FA) and, after a comprehensive study of their properties, determined their photocatalytic properties in reaction of hydrogen evolution in two different electrolytes: aqueous methanolic solution and HI/H_3PO_2 electrolyte. For two of these perovskites, $Rb_3Bi_2I_9$ and $FA_3Bi_2I_9$, the photocatalytic ability was estimated for the first time and were found to be active under UV–Vis light. After 4 h of reaction with the presence of these two perovskites, the efficiency of hydrogen evolution was 31.7 and 20.09 $\mu mol/g_{cat.}$ in MeOH electrolyte and 481.55 and 161.81 $\mu mol/g_{cat.}$ in HI/H_3PO_2 electrolyte. Nevertheless, none of the obtained single perovskites were active under visible light, except for $Cs_3Bi_2I_9$. The efficiency of hydrogen evolution over this photocatalyst under UV–Vis irradiation was determined as 35.47 and 2304.12 $\mu mol/g_{cat.}$ in the methanolic solution and HI/H_3PO_2 electrolyte, respectively, and, under visible light, 10.46 $\mu mol/g_{cat.}$ in HI/H_3PO_2 solution.

Furthermore, our in-depth analysis of the sample after the photoactivity performance proved the destructive effect of the aqueous environment on the perovskite and the high stability in contact with the HI solution. These results provide a better understanding of the reactions and hope for the effective application of such materials in real-world conditions using natural solar irradiation sources.

Because the structure of a single perovskite with Cs cations (in $A_3Bi_2I_9$ type) proved to be the most promising photocatalyst, for the first time and inspired by theoretical research [43–47], we attempted to experimentally obtain double $Cs_2B'BiI_6$ type perovskites (where B′ means Ag, Au, In, or Cu). Unfortunately, it was not possible to obtain double perovskites of this type; instead, a single perovskite, $Cs_3Bi_2I_9$, and an additional crystal phase were obtained. Within this group, the sample with the highest photoactivity was Cs_2AuBiI_6, which was a composite of $Cs_3Bi_2I_9$ and Cs_3IO. In addition to the identification of phases with XRD analysis, XPS also showed the presence of gold in the +3 and + 1 states in that sample. Thus, our results clearly demonstrate that the proposed double perovskite structure of the $Cs_2B'BiI_6$ type (where B′ indicates Ag, Au, In, or Cu) cannot exist under normal conditions because of their decompositive nature [55,77]. However, the as-fabricated composite ($Cs_3Bi_2I_9/Cs_3IO$) proved to be the most active among all the photocatalysts tested in this work, achieving approximately 84.52 and 105.38 μmol/$g_{cat.}$ efficiencies of H_2 production after 4 h of reaction with and without Pt modification in the HI/H_3PO_2 electrolyte, respectively.

Declaration of Competing Interest

The authors declare that they have no known competing financial interests or personal relationships that could have appeared to influence the work reported in this paper.

Data availability

Data will be made available on request.

Acknowledgments

This research was financially supported by the National Science Center of Poland (grant 2018/23/N/ST5/00496: “Metal halide perovskites for heterogeneous photocatalysis”).

Appendix A. Supplementary data

Supplementary data to this article can be found online at https://doi.org/10.1016/j.catcom.2023.106656.

References

[1] A. Zaleska-Medynska, Metal Oxide-Based Photocatalysis: Fundamentals and Prospects for Application, Elsevier, 2018.
[2] X. Yang, D. Wang, Photocatalysis: from fundamental principles to materials and applications, ACS Appl. Energy Mater. 1 (2018) 6657–6693, https://doi.org/10.1021/acsaem.8b01345.
[3] G.L. Chiarello, M.V. Dozzi, E. Selli, TiO_2-based materials for photocatalytic hydrogen production, J. Energy Chem. 26 (2017) 250–258, https://doi.org/10.1016/j.jechem.2017.02.005.
[4] S. Pinilla, A. Machín, S.-H. Park, J.C. Arango, V. Nicolosi, F. Márquez-Linares, C. Morant, TiO_2-based nanomaterials for the production of hydrogen and the development of lithium-ion batteries, J. Phys. Chem. B 122 (2018) 972–983, https://doi.org/10.1021/acs.jpcb.7b07130.
[5] H.H. Do, D.L.T. Nguyen, X.C. Nguyen, T.-H. Le, T.P. Nguyen, Q.T. Trinh, S.H. Ahn, D.-V.N. Vo, S.Y. Kim, Q. Van Le, Recent progress in TiO_2-based photocatalysts for hydrogen evolution reaction: a review, Arab. J. Chem. 13 (2020) 3653–3671, https://doi.org/10.1016/j.arabjc.2019.12.012.
[6] B. Pant, H.R. Pant, M. Park, Y. Liu, J.-W. Choi, N.A.M. Barakat, H.-Y. Kim, Electrospun CdS–TiO_2 doped carbon nanofibers for visible-light-induced photocatalytic hydrolysis of ammonia borane, Catal. Commun. 50 (2014) 63–68, https://doi.org/10.1016/j.catcom.2014.03.002.
[7] S. Taylor, M. Mehta, A. Samokhvalov, Production of hydrogen by glycerol Photoreforming using binary nitrogen–metal-promoted N-M-TiO_2 Photocatalysts, ChemPhysChem. 15 (2014) 942–949, https://doi.org/10.1002/cphc.201301140.
[8] G.L. Chiarello, M.H. Aguirre, E. Selli, Hydrogen production by photocatalytic steam reforming of methanol on noble metal-modified TiO_2, J. Catal. 273 (2010) 182–190, https://doi.org/10.1016/j.jcat.2010.05.012.
[9] A.A. Nada, M.H. Barakat, H.A. Hamed, N.R. Mohamed, T.N. Veziroglu, Studies on the photocatalytic hydrogen production using suspended modified TiO_2 photocatalysts, Int. J. Hydrog. Energy 30 (2005) 687–691, https://doi.org/10.1016/j.ijhydene.2004.06.007.
[10] J.S. Jang, S.M. Ji, S.W. Bae, H.C. Son, J.S. Lee, Optimization of CdS/TiO_2 nano-bulk composite photocatalysts for hydrogen production from Na2S/Na2SO3 aqueous electrolyte solution under visible light (λ≥420nm), J. Photochem. Photobiol. A Chem. 188 (2007) 112–119, https://doi.org/10.1016/j.jphotochem.2006.11.027.
[11] M. Miodyńska, A. Mikolajczyk, B. Bajorowicz, J. Zwara, T. Klimczuk, W. Lisowski, G. Trykowski, H.P. Pinto, A. Zaleska-Medynska, Urchin-like TiO_2 structures decorated with lanthanide-doped Bi2S3 quantum dots to boost hydrogen photogeneration performance, Appl. Catal. B Environ. 272 (2020), 118962, https://doi.org/10.1016/j.apcatb.2020.118962.
[12] G. Malekshoar, A.K. Ray, In-situ grown molybdenum sulfide on TiO_2 for dye-sensitized solar photocatalytic hydrogen generation, Chem. Eng. Sci. 152 (2016) 35–44, https://doi.org/10.1016/j.ces.2016.05.029.
[13] Z. Zhang, S.-W. Cao, Y. Liao, C. Xue, Selective photocatalytic decomposition of formic acid over AuPd nanoparticle-decorated TiO_2 nanofibers toward high-yield hydrogen production, Appl. Catal. B Environ. 162 (2015) 204–209, https://doi.org/10.1016/j.apcatb.2014.06.055.
[14] C. Tedesco, L. Malavasi, Bismuth-based halide perovskites for photocatalytic H_2 evolution application, Molecules. 28 (2023), https://doi.org/10.3390/molecules28010339.
[15] B.M. Bresolin, Y. Park, D.W. Bahnemann, Recent progresses on metal halide perovskite-based material as potential photocatalyst, Catalysts 10 (2020) 1–34, https://doi.org/10.3390/catal10060709.
[16] M.S. Ozório, W.X.C. Oliveira, J.F.R.V. Silveira, A.F. Nogueira, J.L.F. Da Silva, Novel zero-dimensional lead-free bismuth based perovskites: from synthesis to structural and optoelectronic characterization, Mater. Adv. 1 (2020) 3439–3448, https://doi.org/10.1039/D0MA00791A.
[17] Y. Sun, A.J. Fernández-Carrión, Y. Liu, C. Yin, X. Ming, B.-M. Liu, J. Wang, H. Fu, X. Kuang, X. Xing, Bismuth-based halide double perovskite $Cs_2LiBiCl_6$: crystal structure, luminescence, and stability, Chem. Mater. 33 (2021) 5905–5916, https://doi.org/10.1021/acs.chemmater.1c00854.
[18] S. Purohit, K.L. Yadav, S. Satapathi, Metal halide perovskite heterojunction for photocatalytic hydrogen generation: Progress and future opportunities, Adv. Mater. Interfaces 9 (2022) 2200058, https://doi.org/10.1002/admi.202200058.
[19] V. Armenise, S. Colella, F. Fracassi, A. Listorti, Lead-free metal halide perovskites for hydrogen evolution from aqueous solutions, Nanomaterials 11 (2021) 433, https://doi.org/10.3390/nano11020433.
[20] D. Ju, X. Zheng, J. Liu, Y. Chen, J. Zhang, B. Cao, H. Xiao, O.F. Mohammed, O. M. Bakr, X. Tao, Reversible band gap narrowing of Sn-based hybrid perovskite single crystal with excellent phase stability, Angew. Chemie Int. Ed. 57 (2018) 14868–14872, https://doi.org/10.1002/anie.201810481.
[21] Y. Liu, Z. Ma, Combining g-C_3N_4 with $CsPbI_3$ for efficient photocatalysis under visible light, Colloids Surfaces A Physicochem. Eng. Asp. 628 (2021), 127310, https://doi.org/10.1016/j.colsurfa.2021.127310.
[22] L. Ding, C. Shen, Y. Zhao, Y. Chen, L. Yuan, H. Yang, X. Liang, W. Xiang, L. Li, $CsPbBr_3$ nanocrystals glass facilitated with Zn ions for photocatalytic hydrogen production via H_2O splitting, Mol. Catal. 483 (2020), 110764, https://doi.org/10.1016/j.mcat.2020.110764.
[23] W. Song, Y. Wang, C. Wang, B. Wang, J. Feng, W. Luo, C. Wu, Y. Yao, Z. Zou, Photocatalytic hydrogen production by stable $CsPbBr_3$@PANI nanoparticles in aqueous solution, ChemCatChem. 13 (2021) 1711–1716, https://doi.org/10.1002/cctc.202001955.
[24] Y. Wu, P. Wang, Z. Guan, J. Liu, Z. Wang, Z. Zheng, S. Jin, Y. Dai, M.-H. Whangbo, B. Huang, Enhancing the photocatalytic hydrogen evolution activity of mixed-halide perovskite $CH_3NH_3PbBr_3$–xIx achieved by bandgap funneling of charge carriers, ACS Catal. 8 (2018) 10349–10357, https://doi.org/10.1021/acscatal.8b02374.
[25] S. Park, W.J. Chang, C.W. Lee, S. Park, H.-Y. Ahn, K.T. Nam, Photocatalytic hydrogen generation from hydriodic acid using methylammonium lead iodide in dynamic equilibrium with aqueous solution, Nat. Energy 2 (2016) 16185, https://doi.org/10.1038/nenergy.2016.185.
[26] M. Wang, Y. Zuo, J. Wang, Y. Wang, X. Shen, B. Qiu, L. Cai, F. Zhou, S.P. Lau, Y. Chai, Remarkably enhanced hydrogen generation of Organolead halide perovskites via Piezocatalysis and Photocatalysis, Adv. Energy Mater. 9 (2019) 1901801, https://doi.org/10.1002/aenm.201901801.
[27] W. Han, Y. Wei, J. Wan, N. Nakagawa, D. Wang, Hollow multishell-structured $TiO_2/MAPbI_3$ composite improves charge utilization for visible-light photocatalytic hydrogen evolution, Inorg. Chem. 61 (2022) 5397–5404, https://doi.org/10.1021/acs.inorgchem.2c00253.
[28] W. Guan, Y. Li, Q. Zhong, H. Liu, J. Chen, H. Hu, K. Lv, J. Gong, Y. Xu, Z. Kang, M. Cao, Q. Zhang, Fabricating $MAPbI_3/MoS_2$ composites for improved photocatalytic performance, Nano Lett. 21 (2021) 597–604, https://doi.org/10.1021/acs.nanolett.0c04073.
[29] R. Li, X. Li, J. Wu, X. Lv, Y.-Z. Zheng, Z. Zhao, X. Ding, X. Tao, J.-F. Chen, Few-layer black phosphorus-on-$MAPbI_3$ for superb visible-light photocatalytic hydrogen

evolution from HI splitting, Appl. Catal. B Environ. 259 (2019), 118075, https://doi.org/10.1016/j.apcatb.2019.118075.
[30] C. Cai, Y. Teng, J.-H. Wu, J.-Y. Li, H.-Y. Chen, J.-H. Chen, D.-B. Kuang, In situ photosynthesis of an $MAPbI_3$/CoP hybrid heterojunction for efficient photocatalytic hydrogen evolution, Adv. Funct. Mater. 30 (2020) 2001478, https://doi.org/10.1002/adfm.202001478.
[31] Z. Zhao, J. Wu, Y.-Z. Zheng, N. Li, X. Li, X. Tao, Ni_3C-decorated $MAPbI_3$ as visible-light Photocatalyst for H_2 Evolution from HI splitting, ACS Catal. 9 (2019) 8144–8152, https://doi.org/10.1021/acscatal.9b01605.
[32] X. Wang, H. Wang, H. Zhang, W. Yu, X. Wang, Y. Zhao, X. Zong, C. Li, Dynamic interaction between Methylammonium Lead iodide and TiO_2 nanocrystals leads to enhanced photocatalytic H_2 Evolution from HI splitting, ACS Energy Lett. 3 (2018) 1159–1164, https://doi.org/10.1021/acsenergylett.8b00488.
[33] H. Li, X. Lv, R. Li, X. Tao, Y. Zheng, Stable and efficient Ti_3C_2 MXene/$MAPbI_3$-HI system for visible-light-driven photocatalytic HI splitting, J. Power Sources 522 (2022), 231006, https://doi.org/10.1016/j.jpowsour.2022.231006.
[34] J. Yu, X. Xu, Expediting H_2 evolution over $MAPbI_3$ with a nonnoble metal Cocatalyst Mo_2C under visible light, Energy Mater. Adv. 2022 (2022) 9836095, https://doi.org/10.34133/2022/9836095.
[35] T. Zhang, J. Yu, J. Huang, S. Lan, Y. Lou, J. Chen, MoC/$MAPbI_3$ hybrid composites for efficient photocatalytic hydrogen evolution, Dalt. Trans. 50 (2021) 10860–10866, https://doi.org/10.1039/D1DT01809D.
[36] Y. Guo, G. Liu, Z. Li, Y. Lou, J. Chen, Y. Zhao, Stable Lead-free $(CH_3NH_3)_3Bi_2I_9$ perovskite for photocatalytic hydrogen generation, ACS Sustain. Chem. Eng. 7 (2019) 15080–15085, https://doi.org/10.1021/acssuschemeng.9b03761.
[37] G. Chen, P. Wang, Y. Wu, Q. Zhang, Q. Wu, Z. Wang, Z. Zheng, Y. Liu, Y. Dai, B. Huang, Lead-free halide perovskite $Cs_3Bi_{2x}Sb_{2-2x}I_9$ ($x \approx 0.3$) possessing the photocatalytic activity for hydrogen evolution comparable to that of $(CH_3NH_3)PbI_3$, Adv. Mater. 32 (2020) 2001344, https://doi.org/10.1002/adma.202001344.
[38] M. Li, S. Xu, L. Wu, H. Tang, B. Zhou, J. Xu, Q. Yang, T. Zhou, Y. Qiu, G. Chen, G.I. N. Waterhouse, K. Yan, Perovskite $Cs_3Bi_2I_9$ hexagonal prisms with ordered geometry for enhanced photocatalytic hydrogen evolution, ACS Energy Lett. (2022) 3370–3377, https://doi.org/10.1021/acsenergylett.2c01856.
[39] T. Wang, X. Li, Z. Qin, T. Wang, Y. Zhao, Activating photocatalytic hydrogen generation on inorganic lead-free $Cs_2AgBiBr_6$ perovskite via reversible Cu^{2+}/Cu^{+} redox couple, J. Catal. 413 (2022) 509–516, https://doi.org/10.1016/j.jcat.2022.07.009.
[40] Q. Huang, Y. Guo, J. Chen, Y. Lou, Y. Zhao, NiCoP modified lead-free double perovskite $Cs_2AgBiBr_6$ for efficient photocatalytic hydrogen generation, New J. Chem. 46 (2022) 7395–7402, https://doi.org/10.1039/D2NJ00435F.
[41] H. Zhao, K. Chordiya, P. Leukkunen, A. Popov, M. Upadhyay Kahaly, K. Kordas, S. Ojala, Dimethylammonium iodide stabilized bismuth halide perovskite photocatalyst for hydrogen evolution, Nano Res. 14 (2021) 1116–1125, https://doi.org/10.1007/s12274-020-3159-0.
[42] T. Wang, D. Yue, X. Li, Y. Zhao, Lead-free double perovskite $Cs_2AgBiBr_6$/RGO composite for efficient visible light photocatalytic H_2 evolution, Appl. Catal. B Environ. 268 (2020), 118399, https://doi.org/10.1016/j.apcatb.2019.118399.
[43] Z. Xiao, K.-Z. Du, W. Meng, J. Wang, D.B. Mitzi, Y. Yan, Correction to "Intrinsic Instability of $Cs_2In(I)M(III)X_6$ (M = Bi, Sb; X = Halogen) Double Perovskites: A Combined Density Functional Theory and Experimental Study", J. Am. Chem. Soc. 139 (2017) 9409, https://doi.org/10.1021/jacs.7b06199.
[44] H.-J. Feng, W. Deng, K. Yang, J. Huang, X.C. Zeng, Double perovskite Cs_2BBiX_6 (B = Ag, Cu; X = Br, Cl)/TiO_2 heterojunction: an efficient Pb-free perovskite Interface for charge extraction, J. Phys. Chem. C 121 (2017) 4471–4480, https://doi.org/10.1021/acs.jpcc.7b00138.
[45] F. Aslam, H. Ullah, M. Hassan, Theoretical investigation of Cs_2InBiX_6 (X = cl, Br, I) double perovskite halides using first-principle calculations, Mater. Sci. Eng. B 274 (2021), 115456, https://doi.org/10.1016/j.mseb.2021.115456.
[46] H.C. Sansom, G. Longo, A.D. Wright, L.R.V. Buizza, S. Mahesh, B. Wenger, M. Zanella, M. Abdi-Jalebi, M.J. Pitcher, M.S. Dyer, T.D. Manning, R.H. Friend, L. M. Herz, H.J. Snaith, J.B. Claridge, M.J. Rosseinsky, Highly absorbing Lead-free semiconductor Cu_2AgBiI_6 for photovoltaic applications from the quaternary CuI–AgI–BiI_3 phase space, J. Am. Chem. Soc. 143 (2021) 3983–3992, https://doi.org/10.1021/jacs.1c00495.
[47] X.-G. Zhao, J.-H. Yang, Y. Fu, D. Yang, Q. Xu, L. Yu, S.-H. Wei, L. Zhang, Design of Lead-Free Inorganic Halide Perovskites for solar cells via cation-transmutation, J. Am. Chem. Soc. 139 (2017) 2630–2638, https://doi.org/10.1021/jacs.6b09645.
[48] M. Miodyńska, A. Mikolajczyk, P. Mazierski, T. Klimczuk, W. Lisowski, G. Trykowski, A. Zaleska-Medynska, Lead-free bismuth-based perovskites coupled with g–C_3N_4: a machine learning based novel approach for visible light induced degradation of pollutants, Appl. Surf. Sci. 588 (2022), 152921, https://doi.org/10.1016/j.apsusc.2022.152921.
[49] M. Aktary, M. Kamruzzaman, R. Afrose, A comparative study of the mechanical stability, electronic, optical and photocatalytic properties of $CsPbX_3$ (X = cl, Br, I) by DFT calculations for optoelectronic applications, RSC Adv. 12 (2022) 23704–23717, https://doi.org/10.1039/D2RA04591E.
[50] G.M. Paternò, N. Mishra, A.J. Barker, Z. Dang, G. Lanzani, L. Manna, A. Petrozza, Broadband defects emission and enhanced ligand Raman scattering in 0D $Cs_3Bi_2I_9$ colloidal nanocrystals, Adv. Funct. Mater. 29 (2019) 1805299, https://doi.org/10.1002/adfm.201805299.
[51] Z. Li, X. Liu, C. Zuo, W. Yang, X. Fang, Supersaturation-controlled growth of monolithically integrated Lead-free halide perovskite single-crystalline thin film for high-sensitivity photodetectors, Adv. Mater. 33 (2021) 2103010, https://doi.org/10.1002/adma.202103010.
[52] S.S. Bhosale, A.K. Kharade, E. Jokar, A. Fathi, S.M. Chang, E.W.G. Diau, Mechanism of photocatalytic CO_2 reduction by bismuth-based perovskite nanocrystals at the gas-solid Interface, J. Am. Chem. Soc. 141 (2019) 20434–20442, https://doi.org/10.1021/jacs.9b11089.
[53] Y. Zhang, F. Fadaei Tirani, P. Pattison, K. Schenk-Joß, Z. Xiao, M.K. Nazeeruddin, P. Gao, Zero-dimensional hybrid iodobismuthate derivatives: from structure study to photovoltaic application, Dalt. Trans. 49 (2020) 5815–5822, https://doi.org/10.1039/D0DT00015A.
[54] C. Lan, G. Liang, S. Zhao, H. Lan, H. Peng, D. Zhang, H. Sun, J. Luo, P. Fan, Lead-free formamidinium bismuth perovskites $(FA)_3Bi_2I_9$ with low bandgap for potential photovoltaic application, Sol. Energy 177 (2019) 501–507, https://doi.org/10.1016/j.solener.2018.11.050.
[55] Z. Xiao, W. Meng, J. Wang, Y. Yan, Thermodynamic stability and defect chemistry of bismuth-based Lead-free double perovskites, ChemSusChem. 9 (2016) 2628–2633, https://doi.org/10.1002/cssc.201600771.
[56] J. Gu, G. Yan, Y. Lian, Q. Mu, H. Jin, Z. Zhang, Z. Deng, Y. Peng, Bandgap engineering of a lead-free defect perovskite Cs3Bi2I9 through trivalent doping of Ru^{3+}, RSC Adv. 8 (2018) 25802–25807, https://doi.org/10.1039/C8RA04422H.
[57] K.M. McCall, C.C. Stoumpos, O.Y. Kontsevoi, G.C.B. Alexander, B.W. Wessels, M. G. Kanatzidis, From 0D $Cs_3Bi_2I_9$ to 2D $Cs_3Bi_2I_6Cl_3$: dimensional expansion induces a direct band gap but enhances electron–phonon coupling, Chem. Mater. 31 (2019) 2644–2650, https://doi.org/10.1021/acs.chemmater.9b00636.
[58] Y. Zhang, J. Yin, M.R. Parida, G.H. Ahmed, J. Pan, O.M. Bakr, J.-L. Brédas, O. F. Mohammed, Direct-indirect nature of the bandgap in Lead-free perovskite nanocrystals, J. Phys. Chem. Lett. 8 (2017) 3173–3177, https://doi.org/10.1021/acs.jpclett.7b01381.
[59] C.J.P.A.V. Naumkin, A. Kraut-Vass, S.W. Gaarenstroom, NIST X-ray Photoelectron Spectroscopy Database 20. Version 4.1. http://srdata.nist.gov/xps/, 2012.
[60] A. Kanwat, E. Moyen, S. Cho, J. Jang, Rubidium as an alternative cation for efficient perovskite light-emitting diodes, ACS Appl. Mater. Interfaces 10 (2018) 16852–16860, https://doi.org/10.1021/acsami.8b01292.
[61] W.-C. Lin, W.-C. Lo, J.-X. Li, Y.-K. Wang, J.-F. Tang, Z.-Y. Fong, In situ XPS investigation of the X-ray-triggered decomposition of perovskites in ultrahigh vacuum condition, Npj Mater. Degrad. 5 (2021) 13, https://doi.org/10.1038/s41529-021-00162-9.
[62] Y. Jiang, E.J. Juarez-Perez, Q. Ge, S. Wang, M.R. Leyden, L.K. Ono, S.R. Raga, J. Hu, Y. Qi, Post-annealing of $MAPbI_3$ perovskite films with methylamine for efficient perovskite solar cells, Mater. Horizons. 3 (2016) 548–555, https://doi.org/10.1039/C6MH00160B.
[63] S.D. Senanayake, H. Idriss, Photocatalysis and the origin of life: synthesis of nucleoside bases from formamide on TiO_2(001) single surfaces, Proc. Natl. Acad. Sci. 103 (2006) 1194–1198, https://doi.org/10.1073/pnas.0505768103.
[64] J.-Y. Son, T. Mizokawa, J.W. Quilty, K. Takubo, K. Ikeda, N. Kojima, Photoinduced valence transition in gold complexes $Cs_2Au_2X_6$ (X=cl and Br) probed by x-ray photoemission spectroscopy, Phys. Rev. B 72 (2005), 235105, https://doi.org/10.1103/PhysRevB.72.235105.
[65] M.C. Biesinger, L.W.M. Lau, A.R. Gerson, R.S.C. Smart, Resolving surface chemical states in XPS analysis of first row transition metals, oxides and hydroxides: Sc, Ti, V, cu and Zn, Appl. Surf. Sci. 257 (2010) 887–898, https://doi.org/10.1016/j.apsusc.2010.07.086.
[66] J. Zhao, S.C. Nguyen, R. Ye, B. Ye, H. Weller, G.A. Somorjai, A.P. Alivisatos, F. D. Toste, A comparison of photocatalytic activities of gold nanoparticles following Plasmonic and Interband excitation and a strategy for harnessing Interband hot carriers for solution phase Photocatalysis, ACS Cent. Sci. 3 (2017) 482–488, https://doi.org/10.1021/acscentsci.7b00122.
[67] K.K. Mandari, B.S. Kwak, A.K.R. Police, M. Kang, In-situ photo-reduction of silver particles and their SPR effect in enhancing the photocatalytic water splitting of Ag_2O/TiO_2 photocatalysts under solar light irradiation: a case study, Mater. Res. Bull. 95 (2017) 515–524, https://doi.org/10.1016/j.materresbull.2017.08.028.
[68] B. Bajorowicz, A. Mikolajczyk, H.P. Pinto, M. Miodyńska, W. Lisowski, T. Klimczuk, I. Kaplan-Ashiri, M. Kazes, D. Oron, A. Zaleska-Medynska, Integrated experimental and theoretical approach for efficient design and synthesis of gold-based double halide perovskites, J. Phys. Chem. C 124 (2020) 26769–26779, https://doi.org/10.1021/acs.jpcc.0c07782.
[69] M. Tahir, N.S. Amin, Indium-doped TiO_2 nanoparticles for photocatalytic CO2 reduction with H2O vapors to CH4, Appl. Catal. B Environ. 162 (2015) 98–109, https://doi.org/10.1016/j.apcatb.2014.06.037.
[70] H. Sudrajat, M.M. Fadlallah, S. Tao, M. Kitta, N. Ichikuni, H. Onishi, Dopant site in indium-doped $SrTiO_3$ photocatalysts, Phys. Chem. Chem. Phys. 22 (2020) 19178–19187, https://doi.org/10.1039/D0CP02822C.
[71] V. Thi Quyen, K. Jitae, P. Thi Huong, L. Thi Thu Ha, D. My Thanh, N. Minh Viet, P. Quang Thang, Copper doped titanium dioxide as a low-cost visible light photocatalyst for water splitting, Sol. Energy 218 (2021) 150–156, https://doi.org/10.1016/j.solener.2021.02.036.
[72] K. Bhattacharyya, G.P. Mane, V. Rane, A.K. Tripathi, A.K. Tyagi, Selective CO_2 Photoreduction with cu-doped TiO_2 Photocatalyst: delineating the crucial role of cu-oxidation state and oxygen vacancies, J. Phys. Chem. C 125 (2021) 1793–1810, https://doi.org/10.1021/acs.jpcc.0c08441.
[73] J. Zhao, R. Shi, Z. Li, C. Zhou, T. Zhang, How to make use of methanol in green catalytic hydrogen production? Nano Sel. 1 (2020) 12–29, https://doi.org/10.1002/nano.202000010.
[74] A.B. Patil, B.D. Jadhav, P.V. Bhoir, Efficient photocatalytic hydrogen production over Ce/ZnO from aqueous methanol solution, Mater. Renew. Sustain. Energy. 10 (2021) 14, https://doi.org/10.1007/s40243-021-00199-5.

[75] V. Armenise, S. Colella, F. Fracassi, A. Listorti, Lead-free metal halide perovskites for hydrogen evolution from aqueous solutions, Nanomaterials. 11 (2021), https://doi.org/10.3390/nano11020433.
[76] R. Albrecht, H. Menning, T. Doert, M. Ruck, Hydro-flux synthesis and crystal structure of Tl_3IO, Acta Crystallogr. Sect. E Crystallogr. Commun. 76 (2020) 1638–1640, https://doi.org/10.1107/S2056989020012359.
[77] S. Ghosh, H. Shankar, P. Kar, Recent developments of lead-free halide double perovskites: a new superstar in the optoelectronic field, Mater. Adv. 3 (2022) 3742–3765, https://doi.org/10.1039/D2MA00071G.